CrystEngComm

PAPER

View Article Online
View Journal | View Issue

Cite this: *CrystEngComm*, 2024, **26**, 3874

Homochiral hybrid hexagonal antiperovskite crystals [*R*- and *S*-3-chloroquinuclidinium]$_3$($CdCl_3$)($CdCl_4$)†

Zhe-Kun Xu,[a] Jia-Mei Zhang[a] and Zhong-Xia Wang *[b]

Received 19th May 2024,
Accepted 11th June 2024

DOI: 10.1039/d4ce00504j

rsc.li/crystengcomm

Hybrid chiral perovskites with promising optoelectronic and spintronic applications have attracted great attention. However, reports on hybrid chiral antiperovskites have been rare. In this work, we have successfully designed and synthesized a pair of new homochiral hybrid X_3AB-type hexagonal antiperovskite crystals [*R*- and *S*-3-chloroquinuclidinium]$_3$($CdCl_3$)($CdCl_4$) (*R*-1 and *S*-1) by a homochiral strategy. Accordingly, the racemic crystal [3-chloroquinuclidinium]$CdCl_3$ has experienced a significant transformation from an ordinary one-dimensional chain-like hybrid framework to an infrequent hybrid hexagonal antiperovskite structural stacking in homochiral crystals. The enantiomeric relationship between *R*-1 and *S*-1 verified by circular dichroism spectra and their active nonlinear optical intensity indicates the delivery of chirality from organic cations to the entire molecular level. In addition, the representative *R*-1 exhibits an evident thermal anomaly and step-like dielectric response around 406 K, pointing to a possible isomorphic phase transition in *R*-1 and *S*-1. To our knowledge, this is the first report on homochiral hybrid hexagonal antiperovskite crystals. This finding would inspire the design of a novel chiral antiperovskite family by a homochiral strategy.

Introduction

Chirality is widely present in nature and has also integrated into our lives. Most of the drugs developed today are homochiral ones. In materials science, chiral perovskites with inherent inversion symmetry tend to exhibit unique physical and chemical characteristics, including circular dichroism, circularly polarized photoluminescence, nonlinear optics, ferroelectricity, and spintronics, which have been widely studied and applied in various fields.[1–6] ABX_3-type hybrid perovskites as the derived inorganic counterparts by substituted organic cations in the A site and anions in the X site have attracted tremendous attention for various application scenarios in solar cells, light-emitting diodes, sensors, detectors, and other high-tech fields.[7–20] Antiperovskites, just as the name implies, are a subgroup of perovskites with reverse charge distributions. They generally have the formula X_3AB, where the positively charged ions occupy the X site, and the negative ones are in the A and B sites. Since the 1930s, inorganic antiperovskites have been widely studied, showing intriguing performances, such as negative thermal expansion, superconductivity, magnetocaloric effects, *etc.*[21–28] However, traditional inorganic antiperovskites require high-temperature and complex processes for synthesis and are also short of structural diversity. Benefiting from the powerful organic–inorganic hybrid platform, hybrid antiperovskites with new scopes and functions have also shown substantial progress.[25,29,30] In the early stage, known hybrid antiperovskites are limited to a few examples such as ternary tetrathiafulvalenium salts[31] and tris(*N*-ethylpyridinium) (μ_2-oxo)-bis(trichloro-iron) tetrachloro-iron.[32] Subsequently, a series of new hybrid antiperovskite crystals has been acquired under the guidance of Goldschmidt's tolerance factor, which has provided great inspiration for developing a large family of hybrid antiperovskites *via* a chemical substitution path.[33] In particular, hybrid hexagonal antiperovskite structures have successfully achieved unprecedented ferroelectricity based on a rational strategy for molecular ferroelectrics. For example, hybrid hexagonal antiperovskite crystals of $[(CH_3)_3NH]_3(MnX_3)(MnX_4)$ (X = Cl, Br) with quasi-spherical cations were discovered to show rare ferroelectricity coupled with luminescence features.[34,35] In addition, we synthesized a fluorinated hybrid hexagonal antiperovskite molecular ferroelectric $[(CH_3)_2(F\text{-}CH_2CH_2)NH]_3(CdCl_3)(CdCl_4)$ by a H/F substitution strategy, showing a polarization value nearly ten times that of the above antiperovskite ferroelectrics.[36] Further, a trigonal antiperovskite crystal of racemic [*N*,*N*-dimethyl-3-

[a] *Ordered Matter Science Research Center, Nanchang University, Nanchang 330031, People's Republic of China*
[b] *College of Chemistry and Chemical Engineering, Gannan Normal University, Ganzhou 341000, People's Republic of China. E-mail: zhongxiawang@ncu.edu.cn*

† Electronic supplementary information (ESI) available. CCDC 2349410–2349413. Structural images, SHG, TGA, DSC, PXRD, dielectric and crystal tables. For ESI and crystallographic data in CIF or other electronic format see DOI: https://doi.org/10.1039/d4ce00504j

fluoropyrrolidinium]$_3$($CdBr_3$)($CdBr_4$) was synthesized and reported with ferroelasticity, different from the enantiomeric [*N*,*N*-dimethyl-3-fluoropyrrolidinium]$_3CdBr_3$ perovskites.[37] However, synthetic strategies for hybrid antiperovskites are still inadequate, and further discovery of hybrid antiperovskite structures with desired functional features remains a challenge. Very recently, a chiral strategy for homochiral hybrid perovskite ferroelectrics has shown tremendous potential for the highly efficient development of promising multifunctional optoelectronic devices.[38–48] The underlying is mainly attributed to the close relation between chirality and ferroelectricity, because the chirality can ensure the noncentrosymmetric crystallographic point group in crystal, greatly increasing the possibility of ferroelectricity.[48,49] Unfortunately, chiral hybrid antiperovskite crystals are rare.

Herein, we report the design and synthesis of new X_3AB-type hybrid hexagonal antiperovskite enantiomeric crystals *R*-1 and *S*-1 by the introduction of chirality. The racemic 3-chloroquinuclidinium cation with $CdCl_2$ in an aqueous solution showed an ABX_3-type hybrid structure [3-chloroquinuclidinium]$CdCl_3$ (*Rac*-1) including a one-dimensional infinite edge-sharing $CdCl_5$ pyramidal pentahedron in the structure. As the homochiral *R*- and *S*-3-chloroquinuclidinium cations were engaged, a significant structural transformation to a hexagonal antiperovskite was observed, accompanied by chirality and dielectric response (Scheme 1). Both *R*-1 and *S*-1 crystallize in the chiral-polar $P6_3$ space group and show evident SHG intensity, revealing that the chirality from the homochiral organic cations has been transferred to the entire molecular level. To our knowledge, reports on the utilization of a chiral chemical strategy for homochiral hybrid hexagonal antiperovskite crystals are rare. This finding would greatly highlight the rational design of chiral hybrid materials.

Results and discussion

Structural analysis

Rac-1 crystallizes in the monoclinic $P2_1/n$ space group with the crystallographic parameters a = 7.1351(3) Å, b = 24.6782(7) Å, c = 7.2386(3) Å, β = 107.239(4)°, and V = 1217.32(8) Å^3 (Table S1, ESI†). The asymmetric unit of *Rac*-1 consists of an ordered 3-chloroquinuclidinium organic cation and a $[CdCl_3]^-$ inorganic anionic moiety (Fig. 1a). Weak interactions exist between the organic and inorganic parts and show donor–acceptor distances of 3.274(5) Å, 3.433(5) Å and 3.656(5) Å in N–H···Cl hydrogen bonds (Table S2, ESI†). The inorganic $[CdCl_3]^-$ demonstrates infinite edge-sharing $CdCl_5$ pyramidal pentahedra with slight distortion, where the length of Cd–Cl bonds is in the range of 2.4386(13)–2.6797(15) Å and the Cl–Cd–Cl bond angle is between 83.29(4)° and 157.29(4)° (Table S3, ESI†). Therefore, the crystal packing shown in Fig. 1b exhibits a one-dimensional chain-like structure along the *a*-axis.

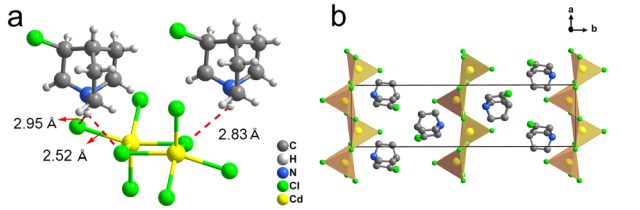

Fig. 1 (a) Molecular structure of *Rac*-1. The red dashed line stands for the hydrogen bond interactions. (b) Packing view of *Rac*-1. H atoms were omitted for clarity.

Subsequently, an attempt to introduce chirality for adjusting the crystal structure and physical properties was carried out. Interestingly, homochiral organic *R*- and *S*-3-chloroquinuclidinium chlorides reacting with $CdCl_2$ exhibit an infrequent hybrid hexagonal antiperovskite structure with the formula X_3AB. Structurally specific, both *R*-1 and *S*-1 crystals possess a chiral-polar hexagonal $P6_3$ space group at room temperature, revealing that the chirality of homochiral organic cations has been transferred into the whole molecular

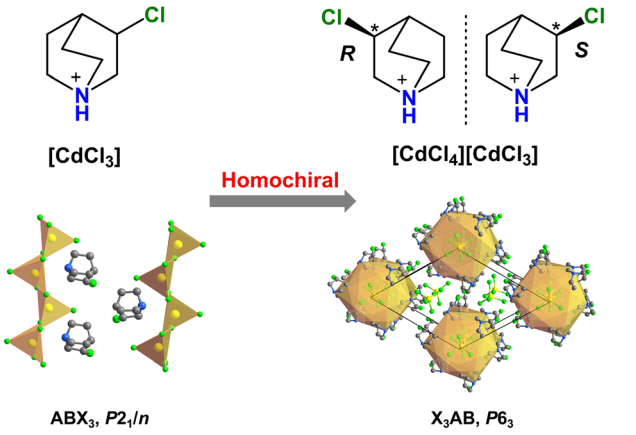

Scheme 1 Homochiral approach for enantiomeric hexagonal antiperovskite crystals.

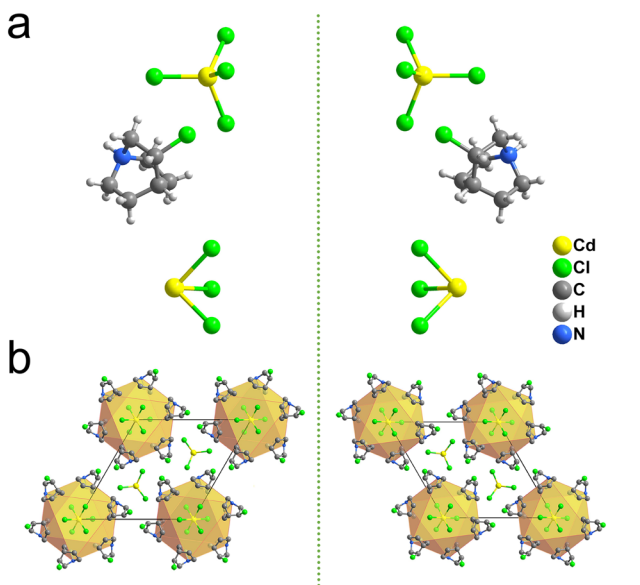

Fig. 2 (a) Asymmetric unit of *R*-1 (right) and *S*-1 (left); (b) packing view of *R*-1 (right) and *S*-1 (left). H atoms were omitted for clarity. The green dashed line denotes the mirror relationship.

framework. The collected diffraction data of enantiomeric crystals were refined to show similar cell parameters in a typical hexagonal symmetry (Table S1, ESI†). Their asymmetric units both contain homochiral organic cations and two kinds of anionic motifs (Fig. 2a). The stacking views of *R*-1 and *S*-1 are shown in Fig. 2b, where the anionic $[CdCl_3]^-$ motif and the ordered organic cations form an infinite one-dimensional chain along the *c*-axis with the tilted face-sharing [*R*- and *S*-3-chloroquinuclidinium]$_6(CdCl_3)$ octahedra. Between the adjacent chains, the embedded space is filled with the tetrahedral $[CdCl_4]^{2-}$ anions. Such a structural stacking model is similar to typical hexagonal perovskite $BaNiO_3$ (Fig. S1, ESI†).[29,50] For *R*-1 and *S*-1, the positively charged organic molecules occupy the position belonging to oxygen atoms in $BaNiO_3$, and the negatively charged $[CdCl_4]^{2-}$ and $[Cd(Cl_{0.5})_6]^-$ parts replace the Ba and Ni sites, respectively. Therefore, both *R*-1 and *S*-1 can be thought of as hexagonal antiperovskite structures and are isomorphic to the previously reported ones, including the similar length of bonds (Cl–Cd) and the angles of adjacent Cl atoms (Cl–Cd–Cl) in inorganic components (Tables S4 and S5, ESI†).[36]

Chiral feature

An enantiomeric feature with a clear mirror relation is observed between the crystal structures of *R*-1 and *S*-1 (Fig. 2), which could be further verified by circular dichroism (CD) and vibrational circular dichroism (VCD) spectra. In Fig. 3a, an evident pair of CD signals at around 247 nm with nearly mirror images was recorded and they are consistent with the UV-vis absorption. The CD signals might result from the cotton effect of chiral inorganic motifs, which is induced by chiral organic cations to produce overall molecular chirality. In addition, VCD spectra were also performed and the results are plotted in Fig. 3b. There are several pairs of strong VCD signals with a mirror at around 1419, 1400, 1386, 1317, 1299, and 978 cm^{-1} corresponding to the infrared peaks in the bottom panel, indicating the enantiomorphic character of *R*-1 and *S*-1. The VCD signal at 1419, 1400, and 1386 cm^{-1} might be attributed to the scissoring vibration of a methylene group, and the peaks at 1317 and 1299 cm^{-1} are possibly due to the rocking vibration of C–H bonds at the chiral center of chiral cations. The information on optical rotations for *R*-1, *S*-1, and their corresponding 3-chloroquinuclidinium chloride have also been investigated and are listed in Table S6 (ESI†), supporting the maintained chirality in antiperovskites. In addition, the second harmonic generation (SHG) signal as a powerful tool to detect the noncentrosymmetric phase should be active to the *R*-1 and *S*-1 with chiral polar point group 6, except for the nonactive point groups 422, 622, and 432 by the Kleiman symmetry rule.[51] In Fig. S2 (ESI†), the SHG intensity of *R*-/*S*-1 is around 0.3 times that of KDP, while *Rac*-1 demonstrates almost zero response.

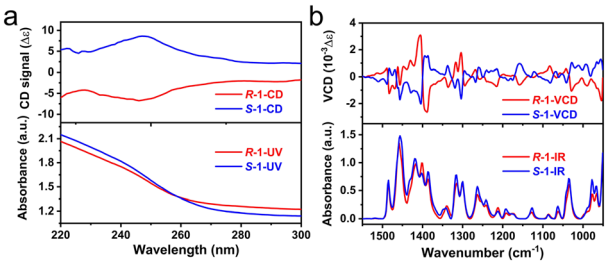

Fig. 3 (a) CD and UV-vis spectra; (b) VCD and IR spectra. The test samples were fabricated using *R*- or *S*-1 and KBr in a mass ratio of 1 : 20.

Thermal and dielectric properties

Thermal stability by thermogravimetric analysis (TGA) shows the decomposition temperature of *R*-1 and *S*-1 up to 480 K and the decomposition point of *Rac*-1 is up to 542 K (Fig. S3, ESI†). Differential scanning calorimetry (DSC) was next performed to detect the thermal anomaly on *R*-1, *S*-1 and *Rac*-1. In Fig. 4(top), prominent thermal peaks around 406 K are observed before the decomposition temperature, revealing the possible phase transition behavior for *R*-1 and *S*-1, but no detected anomaly appears in the DSC curve of *Rac*-1 (Fig. S4a, ESI†). Due to the phase transition temperature approaching the melting point (Fig. S4b, ESI†), it was hard to obtain the structure in the high-temperature phase. In addition, temperature-dependent PXRD measurements of *R*-1 for a representative exhibit that no significant changes occurred around the anomalous temperature, suggesting an isomorphic phase transition (Fig. S5, ESI†). The dielectric constant is generally sensitive to the thermal anomaly behavior. We performed temperature-dependent complex permittivity ε measurements ($\varepsilon = \varepsilon' - i\varepsilon''$, where ε' and ε'' are the real and imaginary parts, respectively) for *R*-1 and *S*-1. As shown in Fig. 4(bottom), both the ε' exhibit an evident step-like change at 1 MHz, gradually increasing from a low dielectric value to a high value of *ca.* 23 and then tends to

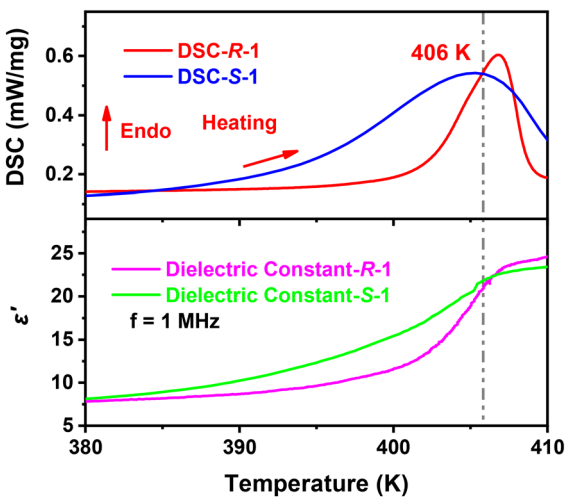

Fig. 4 DSC curves and temperature-dependent dielectric constant at 1 MHz of *R*-1 and *S*-1 in a heating run measured at the rate of 20 K min^{-1}. The amount of powder sample used for the DSC is about 10 mg. For dielectric tests, the powder sample is pressed into sheets of about 0.5 mm.

be stable. It should be noted that the value of ε' significantly increases near the phase transition point under the lower applied dielectric frequencies, exhibiting a significant dielectric frequency dependence (Fig. S6, ESI†).

Conclusions

In summary, we have successfully synthesized a pair of new homochiral hybrid hexagonal antiperovskite crystals *R*-1 and *S*-1. The racemic [3-chloroquinuclidinium]$CdCl_3$ crystallizes in the monoclinic $P2_1/n$ space group and demonstrates a one-dimensional chain-like structure with infinite edge-sharing $CdCl_5$ pyramidal pentahedra, in which the organic cations are in the A site of the ABX_3 structure. With the introduction of chirality, the structural framework is exceptionally changed to a hexagonal antiperovskite model of the formula X_3AB with the chiral organic cations occupying the X site. *R*-1 and *S*-1 have a high crystallographic symmetry with a chiral polar point group of 6, indicating that the chirality of organic cations has been delivered to the entire molecular structure. The chiral enantiomer relationship of *R*-1 and *S*-1 has been well verified by CD and VCD spectra. In addition, the representative *R*-1 shows a significant thermal anomaly coupled with a step-like dielectric response around 406 K, revealing a possible isomorphic phase transition in *R*-1 and *S*-1. This work highlights the chiral strategy for the efficient construction of chiral functional molecular materials in the future.

Experimental

Materials

rac-3-Quinuclidinol, (*R*)-(−)-3-quinuclidinol, and (*S*)-(+)-3-quinuclidinol were purchased from Heowns. Thionyl chloride ($SOCl_2$), cadmium chloride ($CdCl_2{\cdot}2.5H_2O$), and concentrated hydrochloric acid (36 wt%) were purchased from Macklin. All the reagents were of analytical grade and used without further purification.

Synthesis

The general synthesis procedure for 3-chloroquinuclidinium chloride: *rac*-3-quinuclidinol (100 mmol, 12.79 g) was slowly added into $SOCl_2$ solution (100 ml, 1.68 mol) in a single-necked flask with an ice-water bath. Then the reaction solution was stirred at 80 °C with refluxing for over 7 days. Subsequently, the solvent was removed by evaporation and the crude product was dried in an oven at 60 °C. The target *rac*-3-chloroquinuclidinium chloride could be obtained by recrystallizing with isopropanol (yield 38%). *R*-3-Chloroquinuclidinium chloride (yield 35%) and *S*-3-chloroquinuclidinium chloride (yield 30%) were synthesized using a similar procedure to that of the racemic one. The crystal structure of *R*-3-chloroquinuclidinium chloride is shown in Fig. S7 (ESI†) as a representative. Its refined data are shown in Table S1 (ESI†). PXRD shown in Fig. S8 (ESI†) indicates the purity of the sample, which can be directly used in the next step.

The general synthesis procedure for *Rac*-1, *R*-1 and *S*-1: *rac*-3-chloroquinuclidinium chloride (5 mmol, 0.907 g) and $CdCl_2{\cdot}2.5H_2O$ (5 mmol, 1.142 g) were mixed in concentrated hydrochloric acid solution (10 ml). Transparent single crystals of *Rac*-1 were collected by slow evaporation of the solution on a hot plate at 45 °C (yield 62%). A similar procedure was applied for *R*-1 and *S*-1. Homochiral 3-chloroquinuclidinium chloride (6 mmol, 1.089 g) and $CdCl_2{\cdot}2.5H_2O$ (4 mmol, 0.913 g) were mixed in concentrated hydrochloric acid solution (10 ml). Transparent single crystals of *R*-1 (yield 68%) and *S*-1 (yield 56%) were collected by slow evaporation of the solution on a hot plate at 45 °C. The crystal purity of *Rac*-1, *R*-1, and *S*-1 can be found in Fig. S9 (ESI†).

Methods

A Rigaku CCD diffractometer with Mo-Kα radiation (λ = 0.71073 Å) and Cu-Kα radiation (λ = 1.5418 Å) was used to collect single-crystal structures. The diffraction data were refined by full-matrix least-squares refinements on F^2 with the SHELXL-2014/7 software package (Sheldrick, 2014). All the non-H atoms were refined anisotropically with all reflections of $I > 2\sigma(I)$. All the H atoms could be found in the various maps. DSC measurement was performed on a PerkinElmer Diamond DSC instrument. The powder sample for DSC was studied by heating at a rate of 20 K min^{-1} in a nitrogen atmosphere. Thermogravimetric analysis was carried out with a PerkinElmer TGA 8000 instrument at a rate of 20 K min^{-1} in a nitrogen atmosphere. Complex dielectric permittivity measurements were performed with a TH2828A impedance analyzer over the frequency range from 500 Hz to 1 MHz. The applied electric field is around 0.5 V. Second harmonic generation (SHG) measurements were performed on an INSTEC instrument (pulsed Nd: YAG laser with a wavelength of 782 nm, 1.6 MW peak power, 5 ns pulse duration). Powder X-ray diffraction (PXRD) patterns were determined using a Bruker AXS D8 ADVANCE X-ray diffractometer with Cu-Kα radiation (λ = 0.15406 nm, 40 kV and 30 mA) in the angle range from 5° to 50° with a step size of 0.02°. CD spectra were measured using a JASCO J-1700 spectrometer with the KBr pellet method for the transmission mode test. VCD and IR spectra were measured with a Bruker INVENIO spectrometer equipped with a PMA-50 module. Optical rotations were measured in a 0.02 g ml^{-1} solution under Na D radiation (λ = 589.3 nm) using a Shanghai Jiahang Digipol-P610 polarimeter. All the results are the average values of ten tests.

Data availability

All data generated and analyzed in this study are included in the article and its ESI.† The crystal structures for *R*-3-chloroquinuclidinium chloride, *Rac*-1, *R*-1, and *S*-1 generated in this study have been deposited in the Cambridge

Crystallographic Data Centre under accession code CCDC: 2349410–2349413.

Author contributions

Z.-K. X. and J.-M. Z synthesized the samples and carried out the general characterization. Z.-X. W. conceived the study and wrote the manuscript with input from other authors.

Conflicts of interest

There are no conflicts to declare.

Acknowledgements

This work was supported by the National Natural Science Foundation of China (22222502, 21905126 and 92156015).

References

1 Y. Y. Dang, X. L. Liu, B. Q. Cao and X. T. Tao, *Matter*, 2021, **4**, 794–820.
2 G. K. Long, R. Sabatini, M. I. Saidaminov, G. Lakhwani, A. Rasmita, X. G. Liu, E. H. Sargent and W. B. Gao, *Nat. Rev. Mater.*, 2020, **5**, 423–439.
3 Y. Z. Dong, Y. P. Zhang, X. Y. Li, Y. Q. Feng, H. Zhang and J. L. Xu, *Small*, 2019, **15**, 1902237.
4 C. Chen, L. Gao, W. R. Gao, C. Y. Ge, X. Du, Z. Li, Y. Yang, G. D. Niu and J. Tang, *Nat. Commun.*, 2019, **10**, 1927.
5 C. Q. Yuan, X. Y. Li, S. Semin, Y. Q. Feng, T. Rasing and J. L. Xu, *Nano Lett.*, 2018, **18**, 5411–5417.
6 J. Ahn, E. Lee, J. Tan, W. Yang, B. Kim and J. Moon, *Mater. Horiz.*, 2017, **4**, 851–856.
7 J. Y. Shao, D. M. Li, J. J. Shi, C. Ma, Y. S. Wang, X. M. Liu, X. Y. Jiang, M. M. Hao, L. Z. Zhang, C. Liu, Y. T. Jiang, Z. H. Wang, Y. W. Zhong, S. F. Liu, Y. H. Mai, Y. S. Liu, Y. X. Zhao, Z. J. Ning, L. Z. Wang, B. M. Xu, L. Meng, Z. Q. Bian, Z. Y. Ge, X. W. Zhan, J. B. You, Y. F. Li and Q. B. Meng, *Sci. China: Chem.*, 2023, **66**, 10–64.
8 T. Vijayakanth, D. J. Liptrot, E. Gazit, R. Boomishankar and C. R. Bowen, *Adv. Funct. Mater.*, 2022, **32**, 2109492.
9 L. Mao, J. Chen, P. Vishnoi and A. K. Cheetham, *Acc. Mater. Res.*, 2022, **3**, 439–448.
10 A. Younis, C. H. Lin, X. W. Guan, S. Shahrokhi, C. Y. Huang, Y. T. Wang, T. Y. He, S. Singh, L. Hu, J. R. D. Retamal, J. H. He and T. Wu, *Adv. Mater.*, 2021, **33**, 2005000.
11 X. K. Liu, W. D. Xu, S. Bai, Y. Z. Jin, J. P. Wang, R. H. Friend and F. Gao, *Nat. Mater.*, 2021, **20**, 10–21.
12 S. Shahrokhi, W. X. Gao, Y. T. Wang, P. R. Anandan, M. Z. Rahaman, S. Singh, D. Y. Wang, C. Cazorla, G. L. Yuan, J. M. Liu and T. Wu, *Small Methods*, 2020, **4**, 2000149.
13 J. Y. Kim, J. W. Lee, H. S. Jung, H. Shin and N. G. Park, *Chem. Rev.*, 2020, **120**, 7867–7918.
14 R. Pandey, G. Vats, J. Yun, C. R. Bowen, A. W. Y. Ho-Baillie, J. Seidel, K. T. Butler and S. I. Seok, *Adv. Mater.*, 2019, **31**, 1807376.
15 A. K. Jena, A. Kulkarni and T. Miyasaka, *Chem. Rev.*, 2019, **119**, 3036–3103.
16 W. Li, Z. M. Wang, F. Deschler, S. Gao, R. H. Friend and A. K. Cheetham, *Nat. Rev. Mater.*, 2017, **2**, 16099.
17 F. P. G. de Arquer, A. Armin, P. Meredith and E. H. Sargent, *Nat. Rev. Mater.*, 2017, **2**, 16100.
18 B. Saparov and D. B. Mitzi, *Chem. Rev.*, 2016, **116**, 4558–4596.
19 J. S. Manser, J. A. Christians and P. V. Kamat, *Chem. Rev.*, 2016, **116**, 12956–13008.
20 M. A. Green, A. Ho-Baillie and H. J. Snaith, *Nat. Photonics*, 2014, **8**, 506–514.
21 T. He, Q. Huang, A. P. Ramirez, Y. Wang, K. A. Regan, N. Rogado, M. A. Hayward, M. K. Haas, J. S. Slusky, K. Inumara, H. W. Zandbergen, N. P. Ong and R. J. Cava, *Nature*, 2001, **411**, 54–56.
22 K. Takenaka and H. Takagi, *Appl. Phys. Lett.*, 2009, **94**, 131904.
23 D. Matsunami, A. Fujita, K. Takenaka and M. Kano, *Nat. Mater.*, 2015, **14**, 73–78.
24 K. W. Shi, Y. Sun, J. Yan, S. H. Deng, L. Wang, H. Wu, P. W. Hu, H. Q. Lu, M. I. Malik, Q. Z. Huang and C. Wang, *Adv. Mater.*, 2016, **28**, 3761–3767.
25 Y. G. Wang, H. Zhang, J. L. Zhu, X. J. Lü, S. Li, R. Q. Zou and Y. S. Zhao, *Adv. Mater.*, 2020, **32**, 1905007.
26 W. Xia, Y. Zhao, F. P. Zhao, K. G. Adair, R. Zhao, S. Li, R. Q. Zou, Y. S. Zhao and X. L. Sun, *Chem. Rev.*, 2022, **122**, 3763–3819.
27 J. W. Luo, Q. Ji, Y. L. Wu, X. Y. Gao, J. L. Wang and M. G. Ju, *Mater. Horiz.*, 2023, **10**, 1678–1688.
28 M. J. Li, X. Zhang, Z. Y. Xiong, Y. Q. Li, Y. Zhou, X. Chen, Y. P. Song, M. C. Hong, J. H. Luo and S. E. Zhao, *Angew. Chem., Int. Ed.*, 2022, **61**, e202211151.
29 S. V. Krivovichev, *Coord. Chem. Rev.*, 2024, **498**, 215484.
30 J. Gebhardt and A. M. Rappe, *ACS Energy Lett.*, 2017, **2**, 2681–2685.
31 P. Batail, C. Livage, S. S. P. Parkin, C. Coulon, J. D. Martin and E. Canadell, *Angew. Chem., Int. Ed. Engl.*, 1991, **30**, 1498–1500.
32 K. Zhou, J. Huang and G. Chen, *Huaxue Tongbao*, 1983, **11**, 15–16.
33 C. Shi, H. Yu, Q. W. Wang, L. Ye, Z. X. Gong, J. J. Ma, J. Y. Jiang, M. M. Hua, C. J. Shuai, Y. Zhang and H. Y. Ye, *Angew. Chem., Int. Ed.*, 2020, **59**, 167–171.
34 Z. H. Wei, W. Q. Liao, Y. Y. Tang, P. F. Li, P. P. Li, H. Cai and R. G. Xiong, *J. Am. Chem. Soc.*, 2018, **140**, 8110–8113.
35 P. F. Li, Y. Y. Tang, W. Q. Liao, P. P. Shi, X. N. Hua, Y. Zhang, Z. H. Wei, H. Cai and R. G. Xiong, *Angew. Chem., Int. Ed.*, 2018, **57**, 11939–11942.
36 Z. X. Wang, Y. Zhang, Y. Y. Tang, P. F. Li and R. G. Xiong, *J. Am. Chem. Soc.*, 2019, **141**, 4372–4378.
37 Y. R. Weng, F. Zhou, Y. Shi, S. Y. Tang, H. P. Lv, M. J. Yang, Y. Y. Tang and Y. Ai, *Inorg. Chem.*, 2023, **62**, 19930–19936.
38 S. Sahoo, P. A. Kothavade, D. R. Naphade, A. Torris, B. Praveenkumar, J. K. Zareba, T. D. Anthopoulos, K. Shanmuganathan and R. Boomishankar, *Mater. Horiz.*, 2023, **10**, 3153–3161.
39 Y. Qin, F. F. Gao, S. H. Qian, T. M. Guo, Y. J. Gong, Z. G. Li, G. D. Su, Y. Gao, W. Li, C. Y. Jiang, P. X. Lu and X. H. Bu, *ACS Nano*, 2022, **16**, 3221–3230.

40 C. C. Fan, X. B. Han, B. D. Liang, C. Shi, L. P. Miao, C. Y. Chai, C. D. Liu, Q. Ye and W. Zhang, *Adv. Mater.*, 2022, **34**, 2204119.
41 Y. Hu, F. Florio, Z. Z. Chen, W. A. Phelan, M. A. Siegler, Z. Zhou, Y. W. Guo, R. Hawks, J. Jiang, J. Feng, L. F. Zhang, B. W. Wang, Y. P. Wang, D. Gall, E. F. Palermo, Z. H. Lu, X. Sun, T. M. Lu, H. Zhou, Y. Ren, E. Wertz, R. Sundararaman and J. Shi, *Sci. Adv.*, 2020, **6**, aay4213.
42 C. K. Yang, W. N. Chen, Y. T. Ding, J. Wang, Y. Rao, W. Q. Liao, Y. Y. Tang, P. F. Li, Z. X. Wang and R. G. Xiong, *Adv. Mater.*, 2019, **31**, 1808088.
43 T. Zhang, K. Xu, J. Li, L. He, D. W. Fu, Q. Ye and R. G. Xiong, *Natl. Sci. Rev.*, 2023, **10**, nwac240.
44 W. F. Deng, Y. X. Li, Y. X. Zhao, J. S. Hu, Z. S. Yao and J. Tao, *J. Am. Chem. Soc.*, 2023, **145**, 5545–5552.
45 Y. L. Zeng, X. Q. Huang, C. R. Huang, H. Zhang, F. Wang and Z. X. Wang, *Angew. Chem., Int. Ed.*, 2021, **60**, 10730–10735.
46 J. X. Gao, W. Y. Zhang, Z. G. Wu, Y. X. Zheng and D. W. Fu, *J. Am. Chem. Soc.*, 2020, **142**, 4756–4761.
47 Y. Y. Tang, Y. Ai, W. Q. Liao, P. F. Li, Z. X. Wang and R. G. Xiong, *Adv. Mater.*, 2019, **31**, 1902163.
48 H. Peng, J. C. Qi, Y. S. Liu, J. M. Zhang, W. Q. Liao and R. G. Xiong, *Chin. J. Chem.*, 2024, **42**, 1133–1144.
49 H. Y. Liu, H. Y. Zhang, X. G. Chen and R. G. Xiong, *J. Am. Chem. Soc.*, 2020, **142**, 15205–15218.
50 J. J. Lander, *Acta Crystallogr.*, 1951, **4**, 148–156.
51 P. P. Shi, Y. Y. Tang, P. F. Li, W. Q. Liao, Z. X. Wang, Q. Ye and R. G. Xiong, *Chem. Soc. Rev.*, 2016, **45**, 3811–3827.